

On the X-ray, optical and radio afterglows of the BdHN I GRB 180720B generated by the synchrotron emission

J. A. RUEDA,^{1,2,3,4,5} LIANG LI,^{1,2,6} R. MORADI,^{1,2,6} R. RUFFINI,^{1,2,7,8} N. SAHAKYAN,^{1,9} AND Y. WANG^{1,2,6}

¹*ICRANet, Piazza della Repubblica 10, I-65122 Pescara, Italy*

²*ICRA, Dip. di Fisica, Sapienza Università di Roma, Piazzale Aldo Moro 5, I-00185 Roma, Italy*

³*ICRANet-Ferrara, Dip. di Fisica e Scienze della Terra, Università degli Studi di Ferrara, Via Saragat 1, I-44122 Ferrara, Italy*

⁴*Dip. di Fisica e Scienze della Terra, Università degli Studi di Ferrara, Via Saragat 1, I-44122 Ferrara, Italy*

⁵*INAF, Istituto di Astrofisica e Planetologia Spaziali, Via Fosso del Cavaliere 100, 00133 Rome, Italy*

⁶*INAF, Osservatorio Astronomico d'Abruzzo, Via M. Maggini snc, I-64100, Teramo, Italy*

⁷*Université de Nice Sophia-Antipolis, Grand Château Parc Valrose, Nice, CEDEX 2, France*

⁸*INAF, Viale del Parco Mellini 84, 00136 Rome, Italy*

⁹*ICRANet-Armenia, Marshall Baghranian Avenue 24a, Yerevan 0019, Republic of Armenia*

(Revised April 4, 2022)

ABSTRACT

Gamma-ray bursts (GRBs) are systems of unprecedented complexity across all the electromagnetic spectrum, including the radio, optical, X-rays, gamma-rays in the megaelectronvolt (MeV) and gigaelectronvolt (GeV) regime, as well as ultrahigh-energy cosmic rays (UHECRs), each manifested in seven specific physical processes with widely different characteristic evolution timescales ranging from 10^{-14} s to 10^7 s or longer. We here study the long GRB 180720B originating from a binary system composed of a massive CO_{core} of about $10M_{\odot}$ and a companion neutron star (NS). The gravitational collapse of the CO_{core} gives rise to a spinning newborn NS (ν NS), with an initial period of $P_0 = 1$ ms that powers the synchrotron radiation in the radio, optical, and X-ray wavelengths. We here investigate solely the GRB 180720B afterglows and present a detailed treatment of its origin based on the synchrotron radiation released by the interaction of the ν NS and the SN ejecta. We show that in parallel to the X-ray afterglow, the spinning ν NS also powers the optical and radio afterglows and allows to infer the ν NS and ejecta parameters that fit the observational data.

Keywords: gamma-ray bursts: general — gamma-ray burst: individual (GRB 180720B) — magnetic fields — radiation mechanisms: non-thermal

1. INTRODUCTION

GRB 180720B, identified as a binary-driven hypernova of type one (BdHN I) with redshift $z = 0.653$ has an isotropic energy $E_{\text{iso}} = 5.92 \times 10^{53}$ erg (Ruffini et al. 2018b). The BdHN I model explains the subclass of long GRBs with $E_{\text{iso}} \gtrsim 10^{52}$ erg with a binary progenitor consisting of a carbon-oxygen core (CO_{core}) and a neutron star (NS) companion of $\sim 2M_{\odot}$. The gravitational collapse of the CO_{core}, unlike previous considerations purporting the formation of a single black hole (BH) of $\sim 5\text{--}10 M_{\odot}$ (Woosley 1993), creates in this very large explosion a supernova (SN) which gives rise to a new-

born NS (ν NS) of $\sim 1.5 M_{\odot}$. The accretion of SN ejecta onto the companion NS leads to the BH formation. The interaction of the SN ejecta with the ν NS and the companion BH leads to a large number of complementary explosive episodes, which have been gradually identified in the last twenty years (Ruffini et al. 2021). In addition to the X-rays, GeV and sub-TeV afterglows, the presence of the six episodes in GRB 180720B, marked by their specific spectra representing different underlying physical processes, has been confirmed (see Moradi et al. 2021a, hereafter Paper-I):

I) Episode 1 (UPE I): the BH formation and its consequent ultra-relativistic emission (UPE) phase originated from the vacuum polarization with its characteristic Lorentz factor $\Gamma \sim 100$ (Ruffini et al. 2000, 1999). This marks the first manifestation of the BH

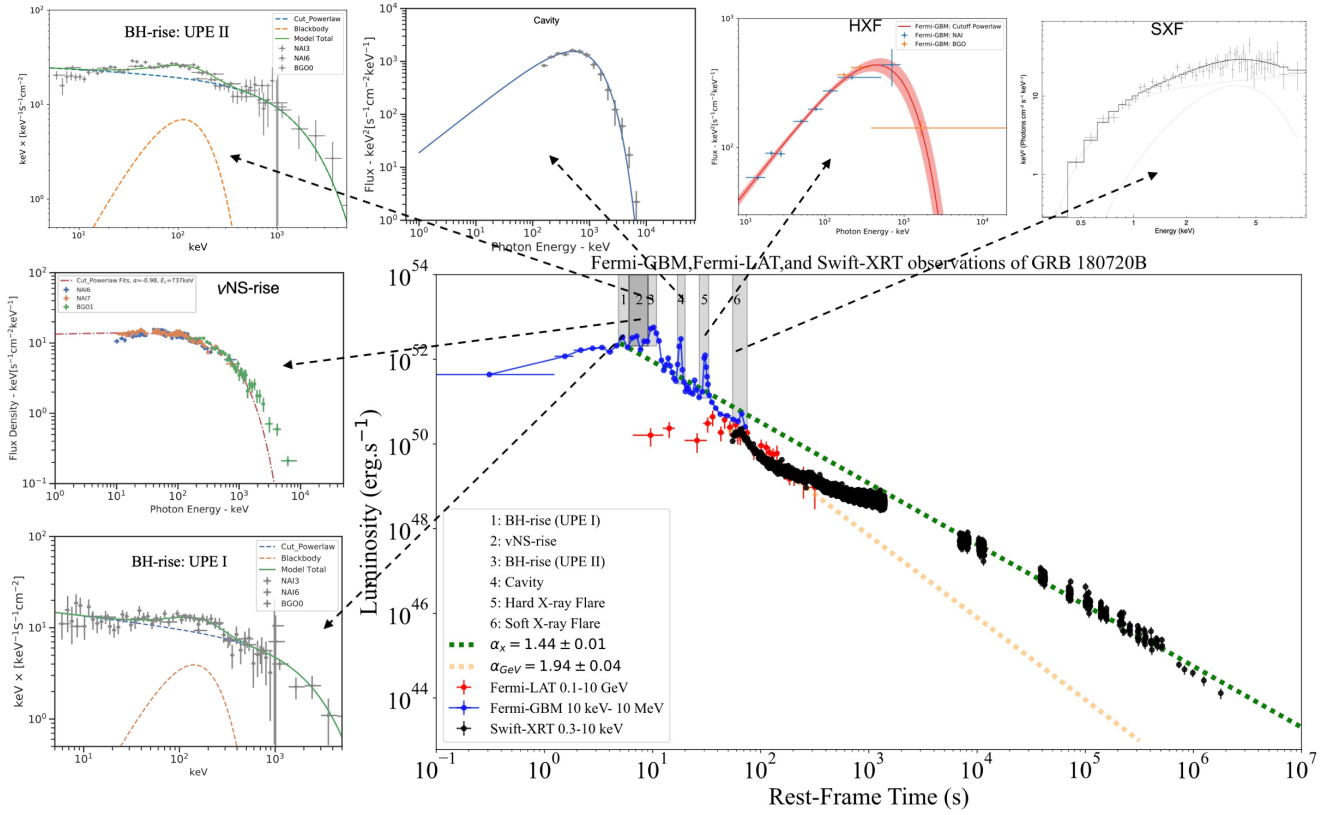


Figure 1. Luminosity light-curve of GRB 180720B and spectra related to the different Episodes identified in GRB 180720B. Plots and best fits are reproduced from Paper-I by the author’s permission.

(BH-rise). In GRB 180720B, the UPE I extends from $t_{\text{rf}} = 4.84$ s to $t_{\text{rf}} = 6.05$ s, its isotropic energy is $E_{\text{UPEI}}^{\text{MeV}} = (6.37 \pm 0.48) \times 10^{52}$ erg, and its spectrum is best fitted by a CPL+BB model (index $\alpha = -1.13$, cut-off energy $E_c = 2220.569$ keV, and blackbody (BB) temperature $kT = 50.31$ keV in the observer’s frame); see Fig 5A in Paper-I.

II) Episode 2 (ν NS-rise): the accretion of ejecta onto the ν NS leads to the ν NS spin-up, which we describe in this article. The first appearance of this interaction in GRB 180720B, referred as the ν NS-rise, extends from $t_{\text{rf}} = 6.05$ s to $t_{\text{rf}} = 9.07$ s, has an isotropic energy of $E_{\nu\text{NS}}^{\text{MeV}} = (1.13 \pm 0.04) \times 10^{53}$ erg, and its spectrum is best fitted by a CPL model ($\alpha = -0.98$, and $E_c = 737$ keV, in the observer’s frame); see Fig. 5B in Paper-I.

III) Episode 3 (UPE II): is marked by the observation of the first significant GeV photon at $t_{\text{rf}} = 7.06$ s, and includes as well the continuation of the UPE phase from $t_{\text{rf}} = 9.07$ s to $t_{\text{rf}} = 10.89$ s, with an isotropic energy of $E_{\text{UPEII}}^{\text{MeV}} = (1.6 \pm 0.95) \times 10^{53}$ erg. The spectrum of the UPE II is best fitted by a CPL+BB model with model

parameters of $\alpha = -1.06^{+0.01}_{-0.01}$, $E_c = 1502.5^{+88.6}_{-87.5}$ keV and $kT = 39.8^{+1.6}_{-1.6}$ keV; see Fig. 5C in Paper-I.

IV) Episode 4 (Cavity): this radiation occurs in the cavity formed during the gravitational collapse of the NS and the consequent BH formation, which becomes further depleted by the UPE phase (Ruffini et al. 2019a). For GRB 180720B, it occurs from $t_{\text{rf}} = 16.94$ s to $t_{\text{rf}} = 19.96$ s, with an isotropic energy of $E_{\text{CV}}^{\text{MeV}} = (4.32 \pm 0.19) \times 10^{52}$ erg, characterized by a CPL spectrum ($\alpha = -1.16$, $E_c = 607.96$ keV). Its spectrum is given in Fig. 5D in Paper-I.

V) Episode 5 (SXF), and VI) Episode 6 (HXF): the interaction of the UPE with the SN ejecta, which has a typical torus-like morphology with a cone of half-opening angle $\sim 60^\circ$ from the normal to the orbital plane (Ruffini et al. (2021), creates the further emission of hard X-ray flare (HXF) and soft X-ray flare (SXF) (Ruffini et al. 2018c). The HXF of GRB 180720B occurs from $t_{\text{rf}} = 28.95$ s to $t_{\text{rf}} = 34.98$ s, with $L_{\text{HXF,iso}}^{\text{MeV}} = (7.8 \pm 0.07) \times 10^{51}$ erg s $^{-1}$, and is best fitted by a CPL model with $E_c = (5.5^{+0.8}_{-0.7}) \times 10^2$ keV, $\alpha = -1.198 \pm 0.031$; see

Fig. 5E in Paper-I. The SXF occurs from $t_{\text{rf}} = 55$ s to $t_{\text{rf}} = 75$ s, with $L_{\text{SXF,iso}}^{\text{X}} = 1.45 \times 10^{50}$ erg, and is best fitted by a PL+BB spectrum with $\alpha = -1.79 \pm 0.23$, and $kT = 0.99 \pm 0.13$ keV; see Fig. 5F in Paper-I.

In GRB 180820B, as indicated in Paper-I, the emission processes originate from three independent energy sources, following the evolution of the progenitors composed of a CO_{core} and companion NS:

1. The SN. As all SNe, it generates a pulsar which here indicated as νNS .
2. The νNS . The first appearance of the νNS (νNS -rise) shows that it has been spun up by fallback accretion of SN ejecta, and is then followed by the late X-ray afterglow with a power-law luminosity $L_X \propto t^{-1.44 \pm 0.01}$. From the energetics of the νNS -rise and the X-ray afterglow, we infer that the νNS period and magnetic field are $P_{\nu\text{NS},0} = 1.01$ ms and $B_{\text{dip}} = 4.2 \times 10^{13}$ G.
3. The BH. The appearance of the BH (BH-rise), formed from the NS companion collapse by accretion of SN ejecta, is marked by the UPE phase followed by the observation of GeV, cavity, HXF and SXF. From the MeV-GeV emission powered by the BH extractable energy, we infer the BH mass $M = 2.4M_{\odot}$, and spin parameter, $\alpha = 0.55$ (see Paper-I).

During the UPE phase of GRB 180720B, the “*inner engine*” of the GRB operates in an overcritical regime. The inner engine consists of a Kerr BH of mass M and angular momentum J , surrounded by a very low-density plasma of ions and electrons with $\rho \sim 10^{-14}$ g cm $^{-3}$ (Ruffini et al. 2019b) in the presence of a uniform magnetic field around the BH, amplified by the gravitational collapse (Rueda et al. 2020). Following the quantum vacuum polarization process in decreasing time bins, we have determined the timescale of the radiation ($\tau \sim 10^{-9}$ s), the Lorentz gamma factors ($\Gamma \sim 30$), the radius of transparency ($R^{\text{tr}} \sim 10^9$ cm), and energy ($E \sim 10^{44}$ erg) of radiation pulses during the UPE phase. The detailed analysis of the UPE phase of GRB 180720B is presented in Rastegarnia, et al., 2022 (submitted). Figure 1 shows the light-curve and spectra of different astrophysical processes underlying different episodes in GRB 180720B; for more details see Paper-I.

In this article, we exclusively analyze the radio, optical, and X-ray afterglows of GRB 180720B. We extend the description of the GRB afterglow developed by Ruffini et al. (2018a) within the BdHN scenario. In this approach, the afterglow originates from the synchrotron radiation produced by the expansion of the SN ejecta in

the presence of the νNS magnetic field. We here provide the theoretical formulation of the underlying synchrotron radiation and demonstrate that the spinning νNS , in addition to the X-ray afterglow, also originates the optical and the radio afterglows.

In addition, we present the fundamental result that in GRB 180720B, Episode VI, namely, the luminosity of the optical SN bump is expected to be comparable to the optical synchrotron radiation. However, no optical data were observed at the time of ~ 15 –20 day after the trigger as we predicted in Ruffini et al. (2018b); see Fig. 2.

The article is organized as follows. In section 2, we represent the X-ray, optical and radio afterglow data of GRB 180720B. In section 3, we represent the formulation related to synchrotron and pulsar radiation of the νNS . In section 4, we represent the concluding remarks.

2. DATA OF GRB 180720B

On 20 July 2018, GRB 180720B triggered Fermi-GBM at 14:21:39.65 UT (Roberts 2018), Swift-BAT at 14:21:44 UT (Siegel 2018), and Fermi-LAT at 14:21:44.55 UT (Bissaldi 2018). Swift-XRT began to observe 91 seconds after the Fermi-GBM trigger (Siegel 2018). These gamma-ray and X-ray data are retrieved and analyzed by Fermi GBM Data Tools (Goldstein et al. 2021) and HEASoft¹ respectively. The corresponding gamma-ray and X-ray luminosity light-curves are shown in 3. This GRB also triggered several optical telescopes. The optical light-curve of r-band in figure 3 is reproduced from Abdalla et al. (2019), which gathers the observations from Kanata (Sasada et al. 2018), MITSuME (Itoh et al. 2018), TSHAO (Reva et al. 2018), MASTER (Lipunov et al. 2018), ISON-Castelgrande (Schmalz et al. 2018), OSN (Kann et al. 2018), LCO (Martone et al. 2018), and KAIT (Zheng & Filippenko 2018).

KAIT provides the latest observation at 3.874 days after the trigger. This time is much ahead of the time of SN optical bump, based on the previous SNe statistics (Cano et al. 2017), and considering this burst occurs at a distance of $z = 0.654$, Ruffini et al. (2018b) predicted that the SN optical flux peaks at 21.8 ± 4.3 days after the trigger. In figure 3, the template SN 1998bw is plotted for comparison, the peak luminosities of other GRB associated SNe vary about 0.5 to 3 times (Cano et al. 2017). The expected optical flux of the SN is not much lower than the optical flux of the synchrotron radiation, the SN signal could be observed if the observation existed at ~ 20 day. We conclude the missing of SN op-

¹ <https://heasarc.gsfc.nasa.gov/heasoft/>

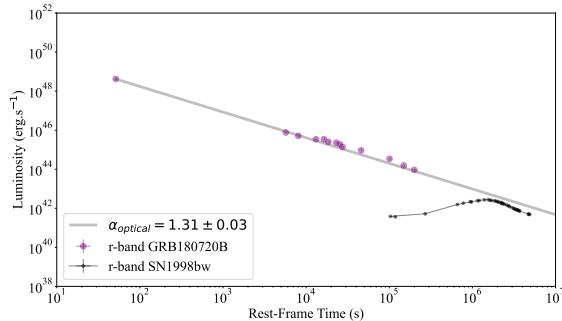


Figure 2. The optical luminosity of prototype SN 1998bw (grey) vs. the optical (purple) afterglow of GRB 180720B. In this GRB, no optical data were observed at the time of ~ 16 – 24 day after the trigger as we predicted in [Ruffini et al. \(2018b\)](#). Most likely, the associated SN could have been detected if optical observations had been made at the time. The r-band optical data retrieved from [Abdalla et al. \(2019\)](#). The optical luminosity of prototype SN 1998bw is plotted from reference ([Iwamoto et al. 1998](#)).

tical signal that we predicted is due to the missing of prolonged optical observations; see Fig. 2.

The GRB 180720B triggered also radio emission observed by Arcminute Microkelvin Imager Large Array (AMI-LA) ([Staley et al. 2012](#); [Anderson et al. 2017](#)). The observed flux which have been made over 5 logarithmically spaced data points, were retrieved from ([Rhodes et al. 2020](#)).

The broad-band luminosity light-curve of GRB 180720B is represented in Fig. 3.

3. SYNCHROTRON AND PULSAR RADIATION OF THE ν NS

We here follow and extend the treatment of the GRB afterglow by [Ruffini et al. \(2018a\)](#) within the BdHN scenario. In this picture, the afterglow originates from the synchrotron radiation produced by the expansion of the SN ejecta in presence of the magnetic field of the ν NS. We now estimate the emission generated by the synchrotron mechanism in the X-rays, in the optical, and in the radio, together with the pulsar emission of the ν NS.

3.1. Synchrotron emission by the expanding ejecta

The evolution of the distribution of radiating electrons per unit energy, $N(E, t)$, is determined by the kinetic equation (see, e.g., [Kardashev 1962](#); [Rybicki & Lightman 1979](#))

$$\frac{\partial N(E, t)}{\partial t} = -\frac{\partial}{\partial E} \left[\dot{E} N(E, t) \right] + Q(E, t), \quad (1)$$

where $Q(E, t)$ is the number of injected electrons into the ejecta per unit time t , per unit energy E , and \dot{E} is the electron energy loss rate.

In the present model, the electrons are subjected to adiabatic losses due to the ejecta expansion and synchrotron radiation losses because of the presence of the ν NS magnetic field. The electrons lose their energy efficiently by synchrotron radiation, so we can assume a one-zone model adopting that the emission originates from the innermost layer of the ejecta, which we denote as $r = R_*$. We assume that the ejecta expand at constant velocity $v_{*,0}$, so the radius evolves as

$$R_*(t) = R_{*,0} \hat{t}, \quad (2)$$

where $\hat{t} \equiv t/t_*$, and $t_* \equiv R_{*,0}/v_{*,0}$.

Having specified the pace at which the ejecta expand, we can write the energy balance equation governing the evolution of the electron's energy (see, e.g., [Kardashev 1962](#))

$$-\dot{E} = \frac{E}{t} + P_{\text{syn}}(E, t), \quad (3)$$

where the first term on the right-hand side accounts for expansion, adiabatic losses, and the second term is given by the bolometric synchrotron radiation power (see, e.g., [Longair 2011](#))

$$P_{\text{syn}}(E, t) = \beta B_*^2(t) E^2, \quad (4)$$

where $\beta = 2e^4/(3m_e^4 c^7)$, and $B_*(t)$ is the magnetic field the electrons are subjected to. From the traditional pulsar theory, we expect that beyond the light-cylinder, $r = c/\Omega$, where Ω is the rotation angular velocity of the ν NS, the magnetic field of the ν NS decreases linearly with distance (see, e.g., [Goldreich & Julian 1969](#); [Ostriker & Gunn 1969](#)). Therefore, we adopt that the magnetic field strength at the ejecta position varies with time as

$$B_*(t) = B_{*,0} \frac{R_{*,0}}{R_*} = \frac{B_{*,0}}{\hat{t}}, \quad (5)$$

where $B_i^{(0)}$ is the magnetic field strength at $r = R_{*,0}$, and we have used Eq. (2).

For completing the specification of Eq. (1), we need to introduce the distribution of the injected electrons. We assume the power-law distribution (see, e.g., [Kardashev 1962](#); [Pacini & Salvati 1973](#); [Rybicki & Lightman 1979](#); [Longair 2011](#))

$$Q(E, t) = Q_0(t) E^{-\gamma}, \quad 0 \leq E \leq E_{\text{max}}, \quad (6)$$

where γ and E_{max} are parameters to be determined from the observational data, and $Q_0(t)$ can be related to the

Table 1. The episodes and afterglows of GRB 180720B. This table reports the name, the underlying astrophysical process, the duration (s), the best fit spectrum, the isotropic energy (erg), and the reference for each event in GRB 180720B.

Event	Astrophysical Process	duration(s)	Spectrum	E_{iso} (erg)	Ref
I) BH-rise (UPE I)	Vacuum polarization around BH	1.21	CPL+BB $\alpha = -1.13$, $E_c = 2220.57$ keV $kT = 50.31$ keV	$(6.37 \pm 0.48) \times 10^{52}$	Moradi et al. (2021b)
II) ν NS-rise	Synchrotron radiation powered by ν NS	3.01	CPL $\alpha = -0.98$, $E_c = 737$ keV	$(1.13 \pm 0.04) \times 10^{53}$	Rueda et al. (2020)
III) BH-rise (GeV radiation)	Synchrotron radiation powered by BH	600	CPL $\alpha = -2.0 \pm 0.1$	$(2.2 \pm 0.2) \times 10^{52}$	Ruffini et al. (2019b)
BH-rise (UPE II)	Vacuum polarization around BH	1.82	CPL+BB $\alpha = -1.06$, $E_c = 1502.5$ keV $kT = 39.8$ keV	$(1.6 \pm 0.95) \times 10^{53}$	Moradi et al. (2021b)
IV) Cavity	Radiation from cavity's wall	3.02	CPL $\alpha = -1.16$, $E_c = 607.96$ keV	$(4.32 \pm 0.19) \times 10^{52}$	Ruffini et al. (2019a)
V) HXF	Emission from outer SN layers	6.03	CPL $\alpha = -1.198 \pm 0.031$ $E_c = 550$ keV	$(3.93 \pm 0.33) \times 10^{52}$	Ruffini et al. (2018d)
VI) SXF	Emission from outer SN layers	15.12	CPL+BB $\alpha = -1.79 \pm 0.23$ $kT = 0.99 \pm 0.13$ keV	$(2.89 \pm 0.42) \times 10^{52}$	Ruffini et al. (2018c)
VII) Optical SN	Nickel decay	expected to be $\sim 10^6$	PL	expected to be $\sim 10^{49}$	Not observed for GRB 180720B
X-ray Afterglow	Synchrotron radiation powered by ν NS	$\sim 10^7$	PL	$(2.61 \pm 1.0) \times 10^{52}$	Rueda et al. (2020)
Optical Afterglow	Synchrotron radiation powered by ν NS	$\sim 3 \times 10^5$	PL	$(6.10 \pm 1.0) \times 10^{50}$	Abdalla et al. (2019) This work
sub-TeV emission	Unknown	$\sim 3 \times 10^3$	PL	$(2.40 \pm 1.8) \times 10^{50}$	Abdalla et al. (2019)
Radio Afterglow	Synchrotron radiation powered by ν NS	$\sim 2 \times 10^6$	PL	$(2.21 \pm 0.24) \times 10^{46}$	Rhodes et al. (2020) This work

power released by the ν NS and injected into the ejecta. We adopt an injected power of the form

$$L_{\text{inj}}(t) = L_0 \left(1 + \frac{t}{t_q}\right)^{-k}, \quad (7)$$

where L_0 , t_q , and k are model parameters to be obtained from the fit of the observational data. Therefore, the function $Q_0(t)$ can be found from

$$L_{\text{inj}}(t) = \int_0^{E_{\text{max}}} E Q(E, t) dE = Q_0(t) \frac{E_{\text{max}}^{2-\gamma}}{2-\gamma}, \quad (8)$$

which using Eq. (7) leads to

$$Q_0(t) = q_0 \left(1 + \frac{t}{t_q}\right)^{-k}, \quad (9)$$

where $q_0 \equiv (2 - \gamma)L_0/E_{\text{max}}^{2-\gamma}$.

Having specified the evolution of the ejecta by Eq. (2) and the magnetic field by Eq. (5), as well as the rate of particle injection given by Eqs. (6) and (9), we can now proceed to the integration of the kinetic equation (1).

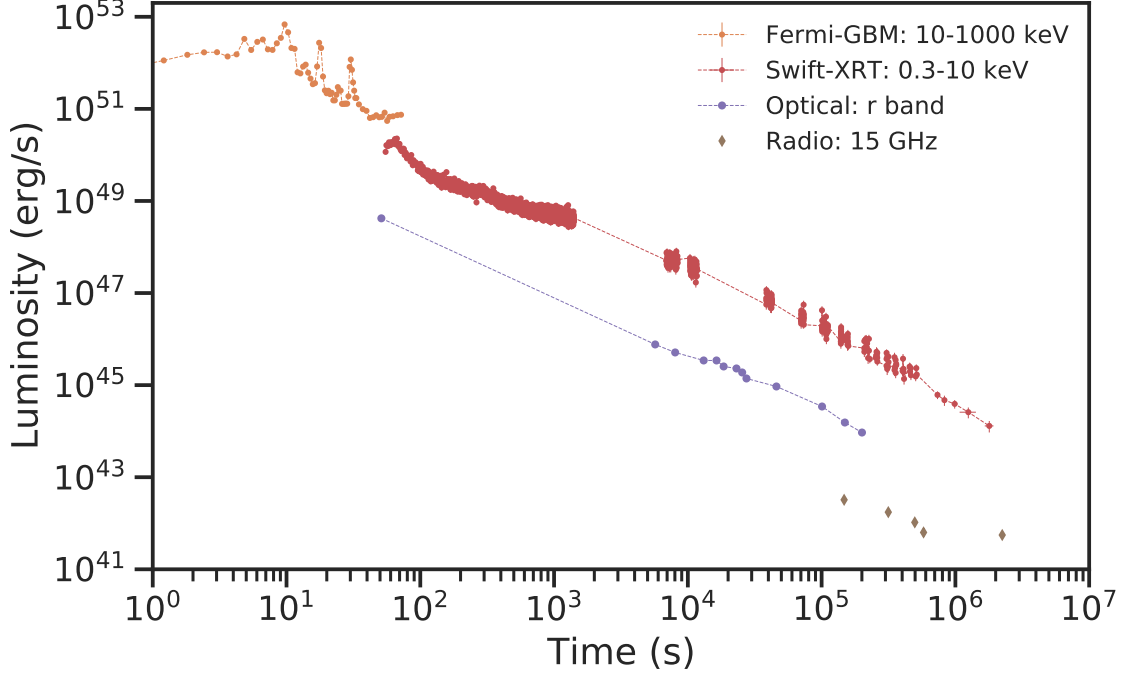


Figure 3. Luminosity light-curve of GRB 180720B: including the observations of gamma-ray from Fermi-GBM (yellow), soft X-ray from Swift-XRT (red), the brown diamonds present the radio data from AMI-LA retrieved from [Rhodes et al. \(2020\)](#), the purple circles represent the r-band optical data retrieved from [Abdalla et al. \(2019\)](#).

First, we find the evolution of a generic electron injected at time $t = t_i$ with energy E_i . Equation (3) can be integrated analytically leading to the energy evolution ([Rueda 2022; Rueda et al. 2022](#))

$$E = \frac{E_i(t_i/t)}{1 + \mathcal{M}E_it_i\left(\frac{1}{t_i^2} - \frac{1}{t^2}\right)}, \quad (10)$$

where $\mathcal{M} \equiv \beta B_{*,0}^2/2$.

The solution of Eq. (1) can be written as (see, e.g., [Pacini & Salvati 1973](#))

$$N(E, t) = \int_E^\infty Q[E_i, t_i(t, E_i, E)] \frac{\partial t_i}{\partial E} dE_i, \quad (11)$$

where $t_i(t, E_i, E)$ is obtained from Eq. (10).

We can write $N(E, t)$ as a piecewise function of time depending upon the behavior of the energy injection (9). All the observational data of GRB 190114C is contained in the regime where synchrotron losses are dominant. In this case, the solution of Eq. (11) is well approximated by ([Rueda 2022](#))

$$N(E, t) \approx \begin{cases} \frac{q_0}{\beta B_{*,0}^{2(\gamma-1)}} \hat{t}^2 E^{-(\gamma+1)}, & t < t_q \\ \frac{q_0(t_q/t_*)^k}{\beta B_{*,0}^{2(\gamma-1)}} \hat{t}^{2-k} E^{-(\gamma+1)}, & t_q < t < t_b, \end{cases} \quad (12)$$

where $E_b < E < E_{\max}$, being

$$E_b = \frac{\hat{t}}{\mathcal{M}t_*}, \quad t_b = t_*^2 \mathcal{M} E_{\max}. \quad (13)$$

The electrons emit most of the synchrotron radiation at frequencies close to the critical frequency $\nu_{\text{crit}} = \alpha B_* E^2$, where $\alpha = 3e/(4\pi m_e^3 c^5)$. Therefore, we can assume $\nu \approx \nu_{\text{crit}}$, so the bolometric synchrotron power (4) can be written approximately in terms of the radiation frequency as

$$P_{\text{syn}}(E, t) \approx P_{\text{syn}}(\nu, t) = \frac{\beta}{\alpha} B_* \nu, \quad (14)$$

and the spectral density, i.e. energy per unit time, per unit frequency, as (see, e.g., [Longair 2011](#))

$$J_{\text{syn}}(\nu, t) \approx P_{\text{syn}}(\nu, t) N(E, t) \frac{dE}{d\nu} \\ = \frac{\beta}{2} \eta \alpha^{\frac{p-3}{2}} B_{*,0}^{\frac{p+1}{2}} \hat{t}^{\frac{2l-p-1}{2}} \nu^{\frac{1-p}{2}}. \quad (15)$$

where we have used $N(E, t) = \eta \hat{t}^l E^{-p}$, being η , l and p , known constants from Eq. (12).

The synchrotron luminosity radiated in the frequencies $[\nu_1, \nu_2]$ can be then obtained as

$$L_{\text{syn}}(\nu_1, \nu_2; t) = \int_{\nu_1}^{\nu_2} J_{\text{syn}}(\nu, t) d\nu \approx \nu J_{\text{syn}}(\nu, t), \quad (16)$$

where $\nu_1 = \nu$, $\nu_2 = \nu + \Delta\nu$, being $\Delta\nu$ the bandwidth. Because J_{syn} shows a power-law behavior in frequency (see Eq. 15), we have used in the second equality of Eq. (16) the approximation $\Delta\nu/\nu \ll 1$. By substituting Eq. (15) into Eq. (17), we obtain that, at the frequency ν , the synchrotron luminosity is given by

$$L_{\text{syn}}(\nu, t) = \frac{\beta}{2} \alpha^{\frac{p-3}{2}} \eta B_{*,0}^{\frac{p+1}{2}} \hat{t}^{\frac{2l-p-1}{2}} \nu^{\frac{3-p}{2}}. \quad (17)$$

Equation (17) implies that the synchrotron radiation follows a power-law behavior both in time and radiation frequency, $L_{\text{syn}} \propto t^{\frac{2l-p-1}{2}} \nu^{\frac{3-p}{2}}$, where $p = \gamma + 1$ and the value of l depend on whether we are in the phase of constant injection or power-law injection (see Eq. 12). Therefore, the synchrotron radiation leads to a *rainbow* luminosity, characterized by the same power-law index in the X-rays, optical, and radio wavelengths (see Fig. 4). This occurs when the system remains over time in the same physical regime, namely when the observational data is contained within times $t < t_b$, and the electron energies are in the range $E_b < E < E_{\text{max}}$, see Eq. (13). Otherwise, the power-law behavior changes when the system makes a transition to a regime of dominance of adiabatic over synchrotron losses. In the present case, we did not find evidence in the GRB afterglow data of the occurrence of the transition to such a physical regime. This implies that the ratio of the luminosity at different frequencies depends only on the power-law index of the injection rate as (Rueda 2022)

$$\frac{L_{\text{syn}}(\nu_1)}{L_{\text{syn}}(\nu_2)} = \left(\frac{\nu_1}{\nu_2}\right)^{\frac{3-p}{2}} = \left(\frac{\nu_1}{\nu_2}\right)^{\frac{2-\gamma}{2}}. \quad (18)$$

Therefore, we can set the value of γ by fitting the observed X-rays to optical luminosity ratio. Once we have fixed γ , the optical (or X-rays) to radio luminosity ratio is also set. Figure 4 shows that the obtained synchrotron luminosity at radio wavelengths also agrees with the observational data. This result implies that the model leads to the correct observed spectrum of the afterglow emission in the wide range of energies from the radio to the X-rays, which strongly support the present scenario.

3.2. Newborn NS evolution and pulsar emission

At some point in the time evolution, when the synchrotron luminosity has fallen sufficiently, the pulsar emission of the ν NS becomes observable. We calculate this emission by adopting a dipole+quadrupole magnetic field model following Pétri (2015). In this model, the total pulsar (spindown) luminosity is given by

$$L_{\text{sd}} = L_{\text{dip}} + L_{\text{quad}} \\ = \frac{2}{3c^3} \Omega^4 B_{\text{dip}}^2 R^6 \sin^2 \chi_1 \left(1 + \xi^2 \frac{16}{45} \frac{R^2 \Omega^2}{c^2}\right), \quad (19)$$

Parameter	Value
γ	1.34
k	1.73
L_0 (10^{50} erg s $^{-1}$)	5.50
E_{max} ($10^4 m_e c^2$)	1.00
t_q (s)	40.00
$R_{*,0}$ (10^{10} cm)	1.99
$v_{*,0}$ (10^9 cm s $^{-1}$)	1.00
$B_{*,0}$ (10^6 G)	2.51
ξ	200.00
B_{dip} (10^{13} G)	1.50
P (ms)	1.00

Table 2. Numerical values of the theoretical model of synchrotron radiation that fit the multiwavelength observational data of GRB 180720B as shown in Fig. 4.

with R the ν NS radius, and ξ defines the quadrupole to dipole strength ratio

$$\xi \equiv \sqrt{\cos^2 \chi_2 + 10 \sin^2 \chi_2} \frac{B_{\text{quad}}}{B_{\text{dip}}}, \quad (20)$$

where the modes can be separated as: $\chi_1 = 0$ and any value of χ_2 for the $m = 0$ mode, $(\chi_1, \chi_2) = (90^\circ, 0^\circ)$ for the $m = 1$ mode, and $(\chi_1, \chi_2) = (90^\circ, 90^\circ)$ for the $m = 2$ mode.

The evolution of the ν NS is calculated from by integrating the energy balance equation

$$-(\dot{W} + \dot{T}) = L_{\text{tot}} = L_{\text{inj}} + L_{\text{sd}}, \quad (21)$$

where W and T are, respectively, the ν NS gravitational and rotational energy.

Table 2 lists the values of the model parameters that fit the afterglow of GRB 180720B in the X-rays, optical, and radio energy bands. Figure 4 shows that the observed afterglow luminosity that fades with time with the same power-law behavior in the X-rays, optical and radio is explained by the synchrotron emission. The synchrotron luminosity in the X-rays decays exponentially after a few 10^2 s, while it keeps its power-law behavior at lower energies. This occurs because around this time the critical synchrotron radiation energy ($h\nu_{\text{crit}}$) falls below the keV range. After this time, the pulsar emission from the ν NS dominates the X-ray emission. This subsequent dominant role of the pulsar emission in powering the observed X-rays emission has allowed us to infer the strength of the dipole and the quadrupole components of the magnetic field, as well as the rotation period of the ν NS. The radio emission shows an excess over the synchrotron emission at a few 10^6 s whose nature is unclear. This excess could be a signature of the SN or the emergence of the ν NS pulsar in the radio wavelengths, but further observational data at longer times

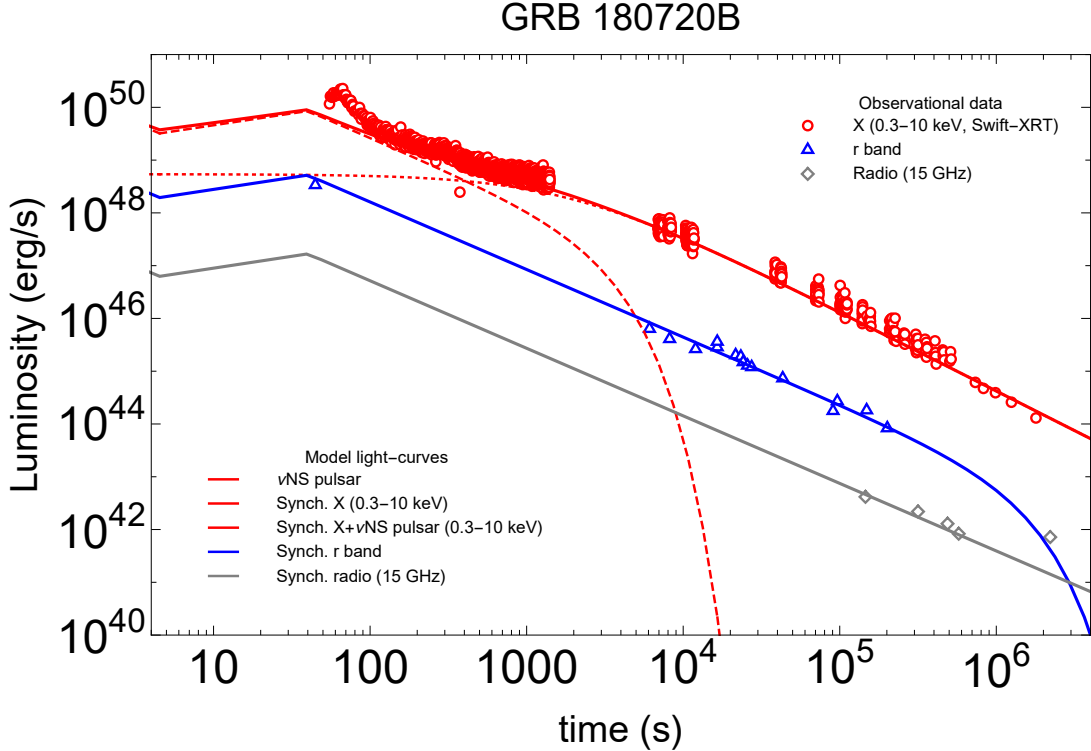


Figure 4. The luminosity of GRB 180720B in the X-rays (0.3–10 keV), optical (r band), and radio (5.0 and 9.0 GHz) energy bands. The X-ray data are produced by the methods developed by the Swift-XRT team to produce the light curves (Evans et al. 2009). The radio data from AMI-LA are retrieved from Rhodes et al. (2020), the r-band optical data are retrieved from Abdalla et al. (2019).

and additional theoretical modeling is needed to confirm or disregard any of these possibilities.

4. CONCLUSIONS

We have pointed out the essential role of the gravitational collapse of the CO_{core} of about $10M_{\odot}$ in presence of a companion NS leading to a variety of independent processes: 1) the SN originated from the CO_{core} collapse, 2) the ejecta accreting on the νNS spins it up to milliseconds and generates the radio, optical and X-ray afterglows, 3) the ejecta accreting onto the companion NS, leading to the BH formation that generates the UPE phase and GeV emission.

We have here addressed the afterglows driving the three different components of X-ray, radio and optical emissions. The synchrotron radiation in the optical wavelengths overcomes most of the optical SN except for the SN peak that could have been barely observed. However, in this case, no observational data were acquired at the needed time of ~ 20 day after the trigger as we predicted in Ruffini et al. (2018b). The associated SN could have been detected if observations at optical wavelengths had been taken at those times.

From the analysis presented in Paper-I, the most general BdHN I, GRB 180720B, comprises seven indepen-

dent Episodes characterized by specific spectral signatures and energetics. They originate from the gravitational collapse of a CO_{core} in the presence of a binary NS companion. Their successful analysis has clarified the occurrence of the most energetic and possibly one of the most complex systems in the Universe. Some Episodes have been observed in selected BdHNe I, e.g., in GRB 190114C (Ruffini et al. 2021), and GRB 130427A (Ruffini et al. 2019b). It is the first time that six of these Episodes have been observed in a single source. This has been made possible by the statistically significant data available and the special inclination of the viewing angle with respect to the equatorial plane of the binary system in GRB 180720B. The latter made possible the observation of the HXF and the SXF. Only the seventh Episode, the final observation of the optical SN due to the nickel decay, with a predicted peak bolometric optical luminosity of $L_{\text{p,avg}} = (8.9 \pm 3.8) \times 10^{42} \text{ erg s}^{-1}$ and rest-frame peak time of $t_{\text{p,avg}} = (1.2 \pm 0.24) \times 10^6 \text{ s}$, was observationally missed.

In summary, the interaction of the SN ejecta with the νNS originated the emission of $(1.39 \pm 0.05) \times 10^{53} \text{ erg}$, revealed in the νNS -rise, and different afterglows in the X-ray, optical, radio and sub-TeV emission. Likewise, an emission of $(1.7 \pm 1.0) \times 10^{53} \text{ erg}$ originates from the

accretion of the SN ejecta onto the companion, fast-spinning magnetized NS, creates the two events of ultra-relativistic jetted emissions (UPE I and UPE II), and the jetted GeV emission; see details in Table 1.

Therefore, BdHNe I are characterized by seven Episodes and four long-lasting emissions in the radio,

optical, X-ray, and GeV bands. The total energy originating into the gravitational collapse of the CO_{core} in GRB 180720B is therefore of $(8.0 \pm 1.0) \times 10^{53}$ erg, which classifies this source as a Giganova.

REFERENCES

- Abdalla, H., Adam, R., Aharonian, F., et al. 2019, *Nature*, 575, 464, doi: [10.1038/s41586-019-1743-9](https://doi.org/10.1038/s41586-019-1743-9)
- Anderson, G. E., Staley, T. D., van der Horst, A. J., et al. 2017, *Monthly Notices of the Royal Astronomical Society*, 473, 1512, doi: [10.1093/mnras/stx2407](https://doi.org/10.1093/mnras/stx2407)
- Bissaldi, E. 2018, GRB Coordinates Network, 22980, 1
- Cano, Z., Wang, S.-Q., Dai, Z.-G., & Wu, X.-F. 2017, *Advances in Astronomy*, 2017, 8929054, doi: [10.1155/2017/8929054](https://doi.org/10.1155/2017/8929054)
- Evans, P. A., Beardmore, A. P., Page, K. L., et al. 2009, *MNRAS*, 397, 1177, doi: [10.1111/j.1365-2966.2009.14913.x](https://doi.org/10.1111/j.1365-2966.2009.14913.x)
- Goldreich, P., & Julian, W. H. 1969, *ApJ*, 157, 869, doi: [10.1086/150119](https://doi.org/10.1086/150119)
- Goldstein, A., Cleveland, W. H., & Kocevski, D. 2021, *Fermi GBM Data Tools: v1.1.0*. <https://fermi.gsfc.nasa.gov/ssc/data/analysis/gbm>
- Itoh, R., Murata, K. L., Tachibana, Y., et al. 2018, GRB Coordinates Network, 22983, 1
- Iwamoto, K., Mazzali, P. A., Nomoto, K., et al. 1998, *Nature*, 395, 672, doi: [10.1038/27155](https://doi.org/10.1038/27155)
- Kann, D. A., Izzo, L., & Casanova, V. 2018, GRB Coordinates Network, 22985, 1
- Kardashev, N. S. 1962, *Soviet Ast.*, 6, 317
- Lipunov, V., Gorbovskoy, E., Tiurina, N., et al. 2018, GRB Coordinates Network, 23023, 1
- Longair, M. S. 2011, *High Energy Astrophysics*
- Martone, R., Guidorzi, C., Kobayashi, S., et al. 2018, GRB Coordinates Network, 22976, 1
- Moradi, R., Li, L., Rueda, J. A., et al. 2021a, arXiv e-prints, arXiv:2103.09158. <https://arxiv.org/abs/2103.09158>
- Moradi, R., Rueda, J. A., Ruffini, R., et al. 2021b, *PhRvD*, 104, 063043, doi: [10.1103/PhysRevD.104.063043](https://doi.org/10.1103/PhysRevD.104.063043)
- Ostriker, J. P., & Gunn, J. E. 1969, *ApJ*, 157, 1395, doi: [10.1086/150160](https://doi.org/10.1086/150160)
- Pacini, F., & Salvati, M. 1973, *ApJ*, 186, 249, doi: [10.1086/152495](https://doi.org/10.1086/152495)
- Pétri, J. 2015, *MNRAS*, 450, 714, doi: [10.1093/mnras/stv598](https://doi.org/10.1093/mnras/stv598)
- Reva, I., Pozanenko, A., Volnova, A., et al. 2018, GRB Coordinates Network, 22979, 1
- Rhodes, L., van der Horst, A. J., Fender, R., et al. 2020, *MNRAS*, 496, 3326, doi: [10.1093/mnras/staa1715](https://doi.org/10.1093/mnras/staa1715)
- Roberts, O. J. 2018, GRB Coordinates Network, 22981, 1
- Rueda, J. A. 2022, arXiv e-prints, arXiv:2202.00316. <https://arxiv.org/abs/2202.00316>
- Rueda, J. A., Ruffini, R., Karlica, M., Moradi, R., & Wang, Y. 2020, *ApJ*, 893, 148, doi: [10.3847/1538-4357/ab80b9](https://doi.org/10.3847/1538-4357/ab80b9)
- Rueda, J. A., Ruffini, R., Li, L., et al. 2022, arXiv e-prints, arXiv:2202.00314. <https://arxiv.org/abs/2202.00314>
- Ruffini, R., Karlica, M., Sahakyan, N., et al. 2018a, *ApJ*, 869, 101, doi: [10.3847/1538-4357/aaeac8](https://doi.org/10.3847/1538-4357/aaeac8)
- Ruffini, R., Melon Fuksman, J. D., & Vereshchagin, G. V. 2019a, *ApJ*, 883, 191, doi: [10.3847/1538-4357/ab3c51](https://doi.org/10.3847/1538-4357/ab3c51)
- Ruffini, R., Salmonson, J. D., Wilson, J. R., & Xue, S. 2000, *A&A*, 359, 855
- Ruffini, R., Salmonson, J. D., Wilson, J. R., & Xue, S.-S. 1999, *A&A*, 350, 334
- Ruffini, R., Aimuratov, Y., Bianco, C. L., et al. 2018b, GRB Coordinates Network, 23019, 1
- Ruffini, R., Becerra, L., Bianco, C. L., et al. 2018c, *ApJ*, 869, 151, doi: [10.3847/1538-4357/aaee68](https://doi.org/10.3847/1538-4357/aaee68)
- Ruffini, R., Wang, Y., Aimuratov, Y., et al. 2018d, *ApJ*, 852, 53, doi: [10.3847/1538-4357/aa9e8b](https://doi.org/10.3847/1538-4357/aa9e8b)
- Ruffini, R., Moradi, R., Rueda, J. A., et al. 2019b, *ApJ*, 886, 82, doi: [10.3847/1538-4357/ab4ce6](https://doi.org/10.3847/1538-4357/ab4ce6)
- . 2021, *MNRAS*, 504, 5301, doi: [10.1093/mnras/stab724](https://doi.org/10.1093/mnras/stab724)
- Rybicki, G. B., & Lightman, A. P. 1979, *Radiative processes in astrophysics*
- Sasada, M., Nakaoka, T., Kawabata, M., et al. 2018, GRB Coordinates Network, 22977, 1
- Schmalz, S., Graziani, F., Pozanenko, A., et al. 2018, GRB Coordinates Network, 23020, 1
- Siegel, M. H. 2018, GRB Coordinates Network, 22973, 1
- Staley, T. D., Titterton, D. J., Fender, R. P., et al. 2012, *Monthly Notices of the Royal Astronomical Society*, 428, 3114, doi: [10.1093/mnras/sts259](https://doi.org/10.1093/mnras/sts259)
- Woosley, S. E. 1993, *ApJ*, 405, 273, doi: [10.1086/172359](https://doi.org/10.1086/172359)
- Zheng, W., & Filippenko, A. V. 2018, GRB Coordinates Network, 23033, 1